

Neural Lagrangian Schrödinger bridge

Takeshi Koshizuka* and Issei Sato†

The University of Tokyo

Abstract

Population dynamics is the study of temporal and spatial variation in the size of populations of organisms and is a major part of population ecology. One of the main difficulties in analyzing population dynamics is that we can only obtain observation data with coarse time intervals from fixed-point observations due to experimental costs or other constraints. Recently, modeling population dynamics by using continuous normalizing flows (CNFs) and dynamic optimal transport has been proposed to infer the expected trajectory of samples from a fixed-point observed population. While the sample behavior in CNF is deterministic, the actual sample in biological systems moves in an essentially random yet directional manner. Moreover, when a sample moves from point A to point B in dynamical systems, its trajectory is such that the corresponding action has the smallest possible value, known as *the principle of least action*. To satisfy these requirements of the sample trajectories, we formulate the Lagrangian Schrödinger bridge (LSB) problem and propose to solve it approximately using neural SDE with regularization. We also develop a model architecture that enables faster computation. Our experiments show that our solution to the LSB problem can approximate the dynamics at the population level and that using the prior knowledge introduced by the Lagrangian enables us to estimate the trajectories of individual samples with stochastic behavior.

1 Introduction

The population dynamics of time-evolving individuals appears in various scientific fields, such as cell population in biology [26, 21], air in meteorology [8], and healthcare statistics [16] in medicine. However, tracking individuals over a long period is often difficult due to experimental costs and other constraints such as privacy issues in the case of human social life. Furthermore, it can sometimes be impossible to track the time evolution. For example, since all cells are destroyed once measured using single-cell RNA sequencing, we cannot analyze the behavior of individual cells over time in cell transcriptome measurements. Instead, we only obtain individual samples from cross-sectional populations without alignment across time steps at a few distinct time points. Under these constraints on data measurements, our goal is to better understand not only the time evolution at the population level, but also the time evolution of individual samples in the populations.

Existing methods attempt to estimate population-level dynamics using a recurrent neural network (RNN) [10] or the Jordan-Kinderlehrer-Otto (JKO) flow [2]. Hashimoto et al. [10] proposed using RNN with noise-based regularization to model the diffusion process described by stochastic differential equations (SDEs). Recent studies have attempted to interpolate the trajectories of individual samples

*koshizuka-takeshi938444@g.ecc.u-tokyo.ac.jp

†sato@g.ecc.u-tokyo.ac.jp

between cross-sectional populations at multiple time points by using optimal transport (OT) [26, 21], or CNF [23]. Using a CNF generates continuous-time non-linear trajectories of individual samples from multiple time points. In addition, Tong et al. [23] proposed a regularization for CNF that encourages a straight trajectory on the basis of OT theory. Since the probability distribution transformation based on ordinary differential equations (ODEs) is used in CNF, the behavior of each sample is described by its initial condition in a completely deterministic manner. However, individual samples in population are known to move stochastically and diffuse in nature, including biological system [14].

To handle the stochastic and complex behavior of individual samples, we propose to model the advection-diffusion processes by using SDEs to describe the time evolution of the sample. Furthermore, on the basis of *the principle of least action*, we estimate the sample trajectories that minimize *action*, defined by the time integral of the Lagrangian determined from the prior knowledge. We formulate this problem as the LSB problem, which is a special case of the stochastic optimal transport (SOT) problem, and propose an approximate solution method Neural Lagrangian Schrödinger bridge (NLSB). In NLSB, we train regularized neural SDE [24, 25, 15] by minimizing the Wasserstein loss between the ground-truth and the predicted population. The Lagrangian design defining regularization allows the sample trajectory to reflect various prior knowledge such as OT, manifold geometry, and local velocity arrows proposed by Tong et al. [23]. In addition, we parameterize a potential function instead of the drift function. Adopting the model architecture of the potential function from OT-Flow [19] will speed up the computation of the gradient of the potential function and the regularization term. As a result, we capture the dynamics at the population level as well as or better than conventional methods, and can more accurately predict the trajectory of individual sample from the population.

In short, our contributions are summarized as follows.

1. We formulate the LSB problem to estimate the stochastic sample trajectory according to the principle of least action.
2. We propose NLSB to approximate the LSB problem efficiently by using neural SDE with regularization on the basis of the prior knowledge introduced by the Lagrangian.
3. Our model architecture of the potential function enables its gradient and diagonal components of the Hessian to be computed explicitly, resulting in fast computation.

2 Background

2.1 Flows regularized by Optimal Transport

A CNFs [4] is a method for learning the continuous transformation between two distributions p and q by modeling the ordinary differential equation (ODE):

$$\frac{d\mathbf{x}(t)}{dt} = \mathbf{v}_\theta(\mathbf{x}, t), \quad \text{subject to } \mathbf{x}(t_0) \sim p, \mathbf{x}(t_1) \sim q.$$

Several regularizations of CNFs that lead to straight trajectories have been proposed on the basis of the OT theory. RNODE [7], OT-Flow [19], and TrajectoryNet [23] introduced a regularization $\tilde{\mathcal{R}}_e$ inspired by the dynamic OT formulation [1]. Potential Flow [27] and OT-Flow modeled the potential function Φ that satisfies $\mathbf{v} = -\nabla\Phi$ instead of modeling the velocity function \mathbf{v} . They also proposed an additional OT-based regularization $\tilde{\mathcal{R}}_h$ derived from the Hamilton–Jacobi–Bellman

(HJB) equation [6] satisfied by the potential function. These OT-based regularizations have resulted in faster CNFs [19, 7] and improved the modeling of cellular dynamics [23].

$$\tilde{\mathcal{R}}_e = \int_{t_0}^{t_1} \int_D \frac{1}{2} \|\mathbf{v}_\theta(\mathbf{x}, t)\|^2 d\rho_t(\mathbf{x}) dt, \quad (1)$$

$$\tilde{\mathcal{R}}_h = \int_{t_0}^{t_1} \int_D \left| \partial_t \Phi_\theta(\mathbf{x}, t) - \frac{1}{2} \|\nabla_{\mathbf{x}} \Phi_\theta(\mathbf{x}, t)\|^2 \right| d\rho_t(\mathbf{x}) dt, \quad (2)$$

where ρ_t is the probability measure of the sample \mathbf{x} at the time t .

2.2 Neural stochastic differential equations

SDE has been used to model real-world random phenomena in a wide range of areas, such as chemistry, biology, mechanics, economics and finance [11]. As an extension of neural ODEs, neural SDE has been proposed to model drift and diffusion functions with neural networks, as shown in the following equation:

$$d\mathbf{X}_t = \mathbf{f}_\theta(\mathbf{X}_t, t)dt + \mathbf{g}_\phi(\mathbf{X}_t, t)d\mathbf{W}_t, \quad (3)$$

where $\{\mathbf{X}_t\}_{t \in [t_0, t_{K-1}]}$ is a continuous \mathbb{R}^d -valued stochastic process, $\mathbf{f}_\theta : \mathbb{R}^d \times [t_0, t_{K-1}] \mapsto \mathbb{R}^d$ is a drift function, $\mathbf{g}_\phi : \mathbb{R}^d \times [t_0, t_{K-1}] \mapsto \mathbb{R}^{d \times m}$ is a diffusion function and $\{\mathbf{W}_t\}_{t \in [t_0, t_{K-1}]}$ is an m -dimensional Brownian motion. Tzen and Raginsky [24, 25] proposed neural SDEs as the continuous limit of deep latent Gaussian models optimized in the framework of variational inference. Li et al. [15] extended the adjoint sensitivity method in neural ODEs to neural SDEs, enabling efficient calculation of gradients. Furthermore, they combined this method with gradient-based stochastic variational inference for latent stochastic differential equations (latent SDEs). Other approaches have been proposed, such as training neural SDEs as generative adversarial networks (GANs) [13] and training methods using score matching [22].

2.3 Stochastic Optimal Transports for Marginal Flows

As a framework for comparing probability distributions, OT theory has many applications in machine learning, such as generative modeling and domain adaptation, and in a wide range of scientific fields, such as single-cell biology and neuroscience. Mikami [17] generalized the OT problem and defined the SOT problem as a random mechanics problem determined by *the principle of least action*. The SOT problem for the case in which the two endpoint marginals are fixed to μ_0 and μ_1 is represented as

$$V(\mu_0, \mu_1) := \inf_{\mathbf{X}} \left\{ \mathbb{E} \left[\int_{t_0}^{t_1} L(t, \mathbf{X}_t; \beta_{\mathbf{X}}(\mathbf{X}_t, t)) dt \right] \middle| \mathbf{X}_t \in \mathcal{A}, \mathbf{X}_{t_0} \sim \mu_0, \mathbf{X}_{t_1} \sim \mu_1 \right\},$$

where $L(t, \mathbf{x}, \mathbf{u}) : [t_0, t_1] \times \mathbb{R}^d \times \mathbb{R}^d \mapsto \mathbb{R}_+$ is continuous and convex in \mathbf{u} . \mathcal{A} is the set of all \mathbb{R}^d -valued, continuous semimartingales $\{\mathbf{X}(t)\}_{t_0 \leq t \leq t_1}$ on a complete filtered probability space such that there exists a Borel measurable $\beta_{\mathbf{X}}(\mathbf{X}_t, t) : \bar{C}([t_0, t_1]) \times [t_0, t_1] \mapsto \mathbb{R}^d$ for which $\omega \mapsto \beta_{\mathbf{X}}(\omega, t)$ is $\mathcal{B}(C([t_0, t_1]); \mathbb{R}^d)_+$ -measurable and $\mathbf{X}(t) = \mathbf{X}(0) + \int_{t_0}^t \beta_{\mathbf{X}}(\mathbf{X}_s, s) ds + \int_{t_0}^t \sigma(\mathbf{X}_s, s) d\mathbf{W}_s$ for all $t \in [t_0, t_1]$ and $E \left[\int_{t_0}^{t_1} \{|\beta(\mathbf{X}_t, t)| + |\sigma(\mathbf{X}_t, t)|^2\} dt \right] < \infty$.

They also introduced another similar version of the SOT for a flow of marginal distributions which satisfies the Fokker–Planck (FP) equation.

$$v(\mu_0, \mu_1) := \inf_{\mathbf{f}, \rho} \left\{ \int_{t_0}^{t_1} \int_{\mathbb{R}^d} L(t, \mathbf{x}; \mathbf{f}(\mathbf{x}, t)) d\rho_t(\mathbf{x}) dt \middle| \rho_{t_k} = \mu_k, (\mathbf{f}, \rho_t) \text{ satisfies the FP equation} \right\}, \quad (4)$$

where ρ_t is the probability measure of the random variable \mathbf{x} at the time t . When $\mathbf{u} \mapsto L$ is quadratic, $V(\mu_0, \mu_1) = v(\mu_0, \mu_1)$ proved in [17]. Especially when $L(t, \mathbf{x}, \mathbf{u}) = \frac{1}{2} \|\mathbf{u}\|^2$, the problem 4 is regarded as stochastic optimal control (SOC) problem [20, 5] with the additional terminal constraint and the special case of Schrödinger bridge (SB) [12] problem. Furthermore, if we assume that the sample motion is deterministic by replacing the FP equation with the continuity equation, the problem (4) is reduced to a dynamic OT formulation proposed by Brenier and Benamou [1].

3 Proposed method

In this section, we first introduce Lagrangian-Schrödinger bridge (LSB) problem. We next present an approximate solution for the LSB problem: Neural Lagrangian Schrödinger bridge (NLSB). Finally, we give specific examples of our methodology for specific use cases.

3.1 Lagrangian Schrödinger bridge

We consider the problem of estimating dynamics at both the population and sample-trajectory levels by using probability densities at two known end points. To solve this problem, we need two pieces of prior knowledge about the target system.

1. The stochastic behavior of individual samples yields the population diffusion phenomenon.
2. Individual samples are encouraged to move according to *the principle of least action*.

The principle of least action states that when a sample moves from point A to point B, its trajectory is such that the corresponding action has the smallest possible value, which is known as a fundamental principle in dynamical systems.

We propose to explicitly model diffusion phenomena as well as drift by using SDEs for the time evolution of the sample and to explore the sample paths that minimize *action* defined by the time integral of the Lagrangian. Later in Section 3.3, we will give some examples of prior information described by the Lagrangian. We formulate this problem as a special case of the SOT problem and call it *the Lagrangian-Schdehlinger Bridge (LSB) problem*.

Definition 1 (LSB problem).

$$\begin{aligned}
& \underset{\theta, \phi}{\text{minimize}} && \int_{t_0}^{t_1} \int_D L(t, \mathbf{x}, \mathbf{f}_\theta(\mathbf{x}, t)) d\rho_t(\mathbf{x}; \theta, \phi) dt, \\
& \text{subject to} && d\mathbf{X}_t = \mathbf{f}_\theta(\mathbf{X}_t, t) dt + \mathbf{g}_\phi(\mathbf{X}_t, t) d\mathbf{W}_t, \\
& && \rho_{t_0} = \mu_0, \rho_{t_1} = \mu_1,
\end{aligned} \tag{5}$$

where ρ_t is the probability measure of the random variable \mathbf{X}_t , depending on the functions \mathbf{f} and \mathbf{g} .

If the Lagrangian $L(t, \mathbf{x}, \mathbf{u}) = \frac{1}{2} \|\mathbf{u}\|^2$ and the class of SDEs to be searched is smaller, the LSB problem reduces to a special case of the SB problem. We discuss this linkage in detail in Appendix C. The LSB problem is more challenging than the SOT problem constrained by the FP equation given by Eq. (4) because the SDE solution needs to reflect both the information of the sample paths and the time evolution of the probability distribution.

3.2 Neural Lagrangian Schrödinger bridge

In this section, we propose to solve the LSB problem by using neural SDEs (3) with regularization. As shown in Eq. (5), the LSB is expressed with optimization over Ito SDE with constraints at time t_0 and t_1 . Relaxing this constraint to minimizing Wasserstein-2 cost at time t_1 , i.e. $\mathcal{W}_2(\mu_1, \|\rho_{t_1})$ makes it possible to approximate the LSB problem by using regularized neural SDEs. We propose to approximate the LSB problem by learning neural SDEs with the gradients of the loss:

$$\mathcal{W}_2(\mu_1, \|\rho_{t_1}) + \mathcal{R}_e(\theta; t_0, t_1) + \mathcal{R}_h(\theta, \phi; t_0, t_1), \quad (6)$$

where \mathcal{R}_e and \mathcal{R}_h are the action cost and the HJB regularization, respectively. Let $D_{i,j}(\cdot; \phi)$ be the entry in the i -th row and j -th column of the diffusion coefficient matrix $\mathbf{D}_\phi = \mathbf{g}_\phi \mathbf{g}_\phi^\top$ and Φ_θ be the potential function satisfying $\mathbf{f}_\theta = [\nabla_{\mathbf{u}} L]^{-1}(-\nabla_{\mathbf{x}} \Phi_\theta)$. Then \mathcal{R}_e and \mathcal{R}_h are defined by

$$\mathcal{R}_e(\theta; t_0, t_1) = \int_{t_0}^{t_1} \int_D L(t, \mathbf{x}, \mathbf{f}_\theta(\mathbf{x}, t)) d\rho_t(\mathbf{x}) dt, \quad (7)$$

$$\mathcal{R}_h(\theta, \phi; t_0, t_1) = \int_{t_0}^{t_1} \int_D \left| \partial_t \Phi_\theta(\mathbf{x}, t) + \frac{1}{2} \sum_{i,j} D_{i,j}(\mathbf{x}, t; \phi) [\nabla_{\mathbf{x}}^2 \Phi_\theta(\mathbf{x}, t)]_{i,j} + h(\mathbf{x}, t) \right| d\rho_t(\mathbf{x}) dt, \quad (8)$$

$$h(\mathbf{x}, t) = L(t, \mathbf{x}, \mathbf{f}_\theta(\mathbf{x}, t)) - \nabla_{\mathbf{u}} L(t, \mathbf{x}, \mathbf{u})|_{\mathbf{u}=\mathbf{f}_\theta(\mathbf{x}, t)}^\top \mathbf{f}_\theta(\mathbf{x}, t).$$

The objective function of the LSB problem with the constraint at time t_1 relaxed by the Wasserstein-2 cost can be described as $\mathcal{R}_e + \lambda \mathcal{W}_2$ where λ is Lagrange multiplier. This objective function can be reinterpreted with \mathcal{W}_2 as the main cost and the action cost \mathcal{R}_e as the regularization.

To find additional equations characterizing the solution, we transform the LSB problem into the SOT problem constrained by the FP equation shown in Eq. (4) using the relationship between the FP equation and Ito SDE. The FP equation corresponding to Ito SDE (3) is represented as

$$\frac{\partial p_t}{\partial t} = -\operatorname{div}(p_t \mathbf{f}_\theta) + \sum_{i,j} \frac{\partial^2}{\partial x_i \partial x_j} [D_{i,j}(\mathbf{x}, t; \phi) p_t(\mathbf{x})], \quad (9)$$

where p_t is the probability density of the probability measure ρ_t . Then, we derive the optimality conditions for the SOT problem (4) by introducing a new Lagrangian \mathcal{L} with a space-time-dependent potential function $\Phi(\mathbf{x}, t)$ (See Appendix A for details). According to the conditions characterizing the saddle-point of the Lagrangian \mathcal{L} , we can derive that the potential function Φ_θ needs to satisfy the relation $\mathbf{f}_\theta = [\nabla_{\mathbf{u}} L]^{-1}(-\nabla_{\mathbf{x}} \Phi_\theta)$ and the HJB equation. Therefore, we model the potential function directly from the above relation instead of the drift function. Furthermore, we propose the HJB regularization \mathcal{R}_h that encourages the potential function to satisfy the HJB equation.

3.3 Examples of Lagrangian in Neural Lagrangian Schrödinger bridge

In this section, we provide the three Lagrangian examples of the NLSB in Table 1 and three use case. The examples demonstrate that the Lagrangian design allows a variety of prior knowledge to be reflected in the sample trajectories.

Potential-free system

Without a specific external force on the individual sample, the principle of least action typically indicates that when a sample moves from point A to point B, it tries to minimize the travel distance in the sense of the Euclidean distance. This means that the drift is encouraged to be linear and the stochastic movement to be small, i.e., the Lagrangian is formulated as $L(t, \mathbf{x}, \mathbf{u}) = \frac{1}{2} \|\mathbf{u}\|^2$.

Table 1: Examples of the Lagrangian in Neural Lagrangian Schrödinger bridge

$L(t, \mathbf{x}, \mathbf{u})$	$\mathbf{f}_\theta(\mathbf{x}, t)$	$h(\mathbf{x}, t)$
$\frac{1}{2} \ \mathbf{u}(\mathbf{x}, t)\ ^2$	$-\nabla_{\mathbf{x}} \Phi_\theta(\mathbf{x}, t)$	$-\frac{1}{2} \ \mathbf{f}_\theta(\mathbf{x}, t)\ ^2$
$\frac{1}{2} \ \mathbf{u}(\mathbf{x}, t)\ ^2 - U(\mathbf{x}) + \frac{1}{2} \ \mathbf{u}(\mathbf{x}, t) - \mathbf{v}(\mathbf{x}, t)\ ^2$	$\frac{1}{2} (\mathbf{v}(\mathbf{x}, t) - \nabla_{\mathbf{x}} \Phi_\theta(\mathbf{x}, t))$	$-U(\mathbf{x}) - \ \mathbf{f}_\theta(\mathbf{x}, t)\ ^2 + \frac{1}{2} \ \mathbf{v}(\mathbf{x}, t)\ ^2$
$\frac{1}{2} \mathbf{u}(\mathbf{x}, t)^\top M(\mathbf{x}) \mathbf{u}(\mathbf{x}, t) - U(\mathbf{x}, t)$	$-M(\mathbf{x})^{-1} \nabla_{\mathbf{x}} \Phi_\theta(\mathbf{x}, t)$	$-U(\mathbf{x}, t) - \frac{1}{2} \mathbf{f}_\theta(\mathbf{x}, t)^\top M(\mathbf{x}) \mathbf{f}_\theta(\mathbf{x}, t)$

Cellular system

Tong et al. [23] proposed to introduce the prior knowledge of manifold geometry and local velocity arrows such as RNA-velocity for modeling cellular systems. In the NLSB, these prior knowledge can be handled consistently by designing the Lagrangian. First, we introduce a density-based penalty to constrain the sample trajectories on the data manifold. We estimate the density function $U(\mathbf{x})$ from the data, e.g., by using kernel density estimation and add it to the Lagrangian. Next, we redefine the velocity regularization, which is formulated as cosine similarity maximization in [23], as a squared error minimization and add it to the Lagrangian as well. Therefore, the Lagrangian for the cellular system is defined by

$$L(t, \mathbf{x}, \mathbf{u}) = \frac{1}{2} \|\mathbf{u}(\mathbf{x}, t)\|^2 - U(\mathbf{x}) + \frac{1}{2} \|\mathbf{u}(\mathbf{x}, t) - \mathbf{v}(\mathbf{x}, t)\|^2, \quad (10)$$

where $\mathbf{v}(\mathbf{x}, t)$ is the reference velocity of the cell at the position \mathbf{x} and the time t .

Random dynamical system

Let $M(\mathbf{x})$ be the mass matrix of the sample which is positive definite, $U(\mathbf{x}, t)$ be the potential energy of the system, and $L(t, \mathbf{x}, \mathbf{u}) = \frac{1}{2} \mathbf{u}(\mathbf{x}, t)^\top M(\mathbf{x}) \mathbf{u}(\mathbf{x}, t) - U(\mathbf{x}, t)$ be the Lagrangian in the generalized coordinate system of the Newtonian dynamical system. Then, the individual samples are encouraged to follow *the equations of motion* of the Newtonian mechanics on average. In practice, we can roughly incorporate information such as obstacles and regions where samples cannot or are likely to exist in the form of potential functions. It is also easy to introduce a potential function estimated by other methods.

4 Implementation Details of Neural Lagrangian Schrödinger bridge

4.1 Training for Neural Lagrangian Schrödinger bridge

In this section, we describe a practical learning method for neural SDEs by minimizing loss (6) using the training data. First, for the data, only individual samples from a cross-sectional population with no alignment across time steps at K separate time points are available. Let $T = \{t_0, \dots, t_{K-1}\}$ be a set of time points and denote the data set at time t_i as \mathcal{X}_{t_i} . Next, we describe how we calculate the loss (6) using the training data $\{\mathcal{X}_{t_i}\}_{t_i \in T}$. The first term, the Wasserstein cost, is computed using the L2-Sinkhorn divergence \bar{W}_ϵ between the observed data and the predicted sample at all observation points in T except the initial point at time t_0 . The Sinkhorn divergence can efficiently approximate the Wasserstein distance and solve the bias problem when using the Sinkhorn algorithm.

The prediction sample is obtained by numerically simulating neural SDE from the training data at one previous time point by a standard SDE solver such as the Euler-Maruyama method. We used the GeomLoss library¹ with default settings for the Sinkhorn divergence calculations. The second and third terms, \mathcal{R}_e and \mathcal{R}_h , are also approximated on the sample paths obtained from the numerical simulations of SDE. Therefore, the computational cost of empirical \mathcal{R}_e and \mathcal{R}_h is not high and can be further accelerated by the model architecture described in the next section. To summarize, we minimize the subsequent loss for the model parameters θ, ϕ .

$$\ell(\theta, \phi) = \sum_{t_k \in T \setminus t_0} \left(\overline{\mathcal{W}}_\epsilon(\mu_k \parallel \rho_{t_k}^{\theta, \phi}) + \lambda_e(t_{k-1}, t_k) \hat{\mathcal{R}}_e(\theta; t_{k-1}, t_k) + \lambda_h(t_{k-1}, t_k) \hat{\mathcal{R}}_h(\theta, \phi; t_{k-1}, t_k) \right),$$

where $\mu_k, \rho_{t_k}^{\theta, \phi}$ are the ground-truth and predicted probability measures at time t_k expressed by data samples, respectively. $\hat{\mathcal{R}}_e(t_{k-1}, t_k)$ and $\hat{\mathcal{R}}_h(t_{k-1}, t_k)$ are empirical quantities computed on the simulated sample paths from t_{k-1} to t_k with data $\forall \mathbf{x}(t_{k-1}) \in \mathcal{X}_{t_{k-1}}$ as the initial value. $\lambda_e(t_{k-1}, t_k)$ and $\lambda_h(t_{k-1}, t_k)$ are the weight coefficients to be tuned that is set for the interval $[t_{k-1}, t_k]$.

4.2 Model architecture selection for speedup

We adopt the model architecture of the potential function Φ_θ proposed by OT-Flow [19] because it has two advantages in our framework. First, it can compute the gradient $\nabla_{\mathbf{x}} \Phi$ explicitly, which enables us to calculate the drift function easily. Second, the model is designed for the fast and exact computation of the diagonal component of the potential function’s Hessian. Moreover, when we assume that the diffusion model’s output is a diagonal matrix, i.e. $\mathbf{g}_\phi(\mathbf{x}, t) \in \mathbb{R}^{d \times d}$ and $\mathbf{g}_{i,j} = 0$ ($i \neq j$), the function \mathbf{D}_ϕ is also a diagonal matrix, and the $\sum_{i,j}$ in the second term of \mathcal{R}_h shown in Eq., (8) turns into the sum of the diagonal components only. Combining these two tricks enables speeding up the computation of \mathcal{R}_h , which requires the expensive computation of the Hessian of the potential function Φ . While this model architecture trick was originally used for speeding up the computation of the Jacobian term in neural ODE maximum likelihood training, we propose to use it as a technique to speed up the computation of \mathcal{R}_h . We use a two-layer fully connected neural network (FCNN) for the diffusion function. We also adopted the device used by Kidger et al. [13] in which the activation function tanh is used after the final layer to prevent the output of the diffusion function from becoming excessively large. For details of the model architecture, see Appendix B.

5 Experiments

We evaluated our methods on two datasets. First, we used artificial synthetic data generated from one-dimensional SDEs, where the predicted trajectory and uncertainty can be compared with the ground-truth and easily evaluated by visualization. Second, we used the evolution of single-cell populations obtained from a developing human embryo system. We set the Lagrangian to $L(t, \mathbf{x}, \mathbf{u}) = \frac{1}{2} \|\mathbf{u}\|^2$ for comparison with OT-based regularization of Eq., (1). We compared our methods against standard neural SDE, OT-Flow [19] and TrajectoryNet [23]. We used the same network as NLSB for the drift and diffusion functions of neural SDE and trained only with Sinkhorn divergence in Eq., (4.1). The model architecture of the OT-Flow potential function was the same as that of our model. The base models of OT-Flow and TrajectoryNet were trained with the standard neural ODEs scheme. +OT represents a model trained with the OT-based regularization defined by Eqs., (1) and (2). We used only $\tilde{\mathcal{R}}_e$ for TrajectoryNet; we used both $\tilde{\mathcal{R}}_e$ and $\tilde{\mathcal{R}}_h$ for OT-Flow. We set

¹<https://www.kernel-operations.io/geomloss/>

the interval-dependent coefficients $\tilde{\lambda}_e(t_{k-1}, t_k)$, $\tilde{\lambda}_h(t_{k-1}, t_k)$ for the OT-based regularization as well as Eq., (4.1). See Appendix D for more details on hyperparameters, learning rates, and optimizers.

5.1 Synthetic Population Dynamics: time-dependent Ornstein–Uhlenbeck process

Data

We used a time-dependent one-dimensional Ornstein–Uhlenbeck (OU) process defined by the following SDE:

$$dX_t = (\mu t - \theta X_t)dt + \left(\frac{2t\sigma}{t_{K-1}}\right)dW_t,$$

where $\mu = 0.4$, $\theta = 0.1$, $\sigma = 0.8$, and $t_{K-1} = 4$. First, we simulated the trajectories of several individuals from $t = 0$ to 4 and then extracted only the data at the time of $T = \{0, 1, 2, 3, 4\}$ as snapshots for training. We generated 2048 and 512 samples for each time point as training and validation data, respectively.

Performance metrics

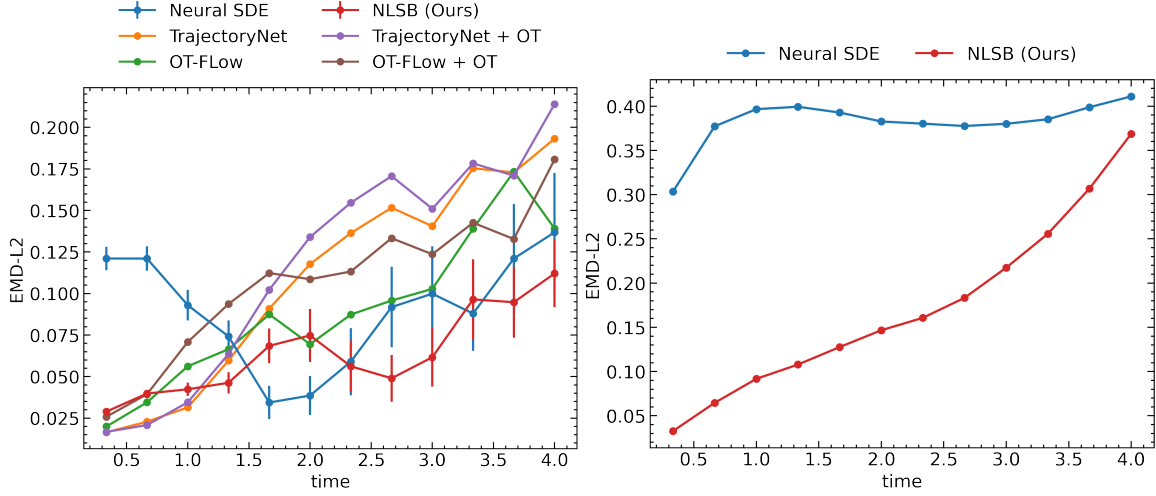
We evaluated the estimation performance of the dynamics in the time interval $[t_0, t_{K-1}]$ by using two metrics: marginal distribution discrepancy (MDD) and conditional distribution discrepancy (CDD).

A smaller MDD between μ_t and ρ_t calculated on the basis of the Wasserstein-2 distance $\mathcal{W}(\mu_t, \rho_t)$ indicates better prediction of population-level dynamics at time t . We calculated MDD at 12 equally spaced time points and the earth mover’s distance with L2 cost (EMD-L2) between 1000 samples generated from the ground-truth SDE and 1000 samples predicted by the model. When evaluating the SDE-based method, we ran 100 simulations from the same initial values, computing the MDD value each time and computing their mean and variance.

A smaller CDD between $\mu_{\mathbf{x}(t)|\mathbf{x}(t_0)}$ and $\rho_{\mathbf{x}(t)|\mathbf{x}(t_0)}$ using the Wasserstein-2 distance $\mathcal{W}(\mu_{\mathbf{x}(t)|\mathbf{x}(t_0)}, \rho_{\mathbf{x}(t)|\mathbf{x}(t_0)})$ indicates better prediction of the distribution followed by the time-evolving samples $\mathbf{x}(t)$ in subsequent time, given the initial state $\mathbf{x}(t_0)$. In short, it is a metric for evaluating the trajectories with uncertainty at the individual data sample level. In the actual CDD calculation, we first prepared 1000 samples $\mathbf{x}(t_0)$ at the initial time point. We then generated 100 trajectories from each initial sample by the trained model and the ground-truth SDE, and calculated the EMD-L2 for the samples from $\mu_{\mathbf{x}(t)|\mathbf{x}(t_0)}$ and $\rho_{\mathbf{x}(t)|\mathbf{x}(t_0)}$ at 12 equally spaced time points. Note that in the case of ODE-based methods such as OT-Flow and TrajectoryNet, we cannot calculate CDD because these methods cannot deal with trajectory uncertainty.

Results

The evaluation results are shown in Figure 1, and the visualization of trajectories is shown in Figure 2. Figures 1 show that NLSB outperforms neural SDE and is comparable to other ODE-based methods in estimating populations with small variance. In contrast, the SDE-based methods outperform ODE-based methods when estimating populations with a large variance. That indicates that NLSB can approximate population-level dynamics even when the population variance is large or small. Furthermore, NLSB has a smaller CDD value than neural SDE. Figure 2b shows that the average behavior of the data samples $E[\hat{X}(t) | X(0)]$ estimated by neural SDE is different from that of the ground-truth SDE (see Figure 2a), especially in the interval $t \in [0, 1]$. In contrast, the estimation by NLSB in Figure 2c is much closer to the ground-truth. These results show that the prior knowledge introduced by the Lagrangian helps to approximate the dynamics at the individual sample level.



(a) MDD at 12 time points on synthetic OU process data. (b) CDD at 12 time points on synthetic OU process data.

Figure 1: Numerical evaluation on synthetic OU process data. All MDD and CDD values were computed between the ground-truth and the estimated samples within generated trajectories all-step ahead from initial samples $\mathbf{x}(t_0)$.

5.2 Single-Cell Population Dynamics

Data

We evaluated on embryoid body single-cell RNA sequencing (scRNA-seq) data [18]. This data shows the differentiation of human embryonic stem cells from embryoid bodies into diverse cell lineages, including mesoderm, endoderm, neuroectoderm, and neural crest, over 27 days. During this period, cells were collected at five different snapshots (t_0 : day 0 to 3, t_1 : day 6 to 9, t_2 : day 12 to 15, t_3 : day 18 to 21, t_4 : day 24 to 27). The collected cells were then measured by scRNAseq, filtered at the quality control stage, and mapped to a low-dimensional feature space using a principal component analysis (PCA). We reused the pre-processed data available in the released repository of TrajectoryNet². For details, see Appendix E.2 in [23]. Following [23], we modeled the trajectory in a five-dimensional PCA space. We split the dataset into train, validation ($\sim 8.5\%$) and test data ($\sim 15\%$).

Performance metrics

Unlike the experiment described in Section 5.1, there are no ground-truth trajectories in the real data. Thus, MDD can be calculated only at the time of observation, and the CDD between the ground truth and predicted trajectories cannot be calculated.

To evaluation of the trajectories, we compared the predicted trajectories when training on all training data and when the model was trained on all but one intermediate snapshot at time t_k . Let \mathcal{D}_{-t_k} be the training data set excluding the intermediate snapshot at time t_k . These trajectories should be similar if the model can estimate the trajectories with good accuracy in the interval where no observational data are available. Therefore, we calculated CDD between the conditional

²<https://github.com/KrishnaswamyLab/TrajectoryNet>

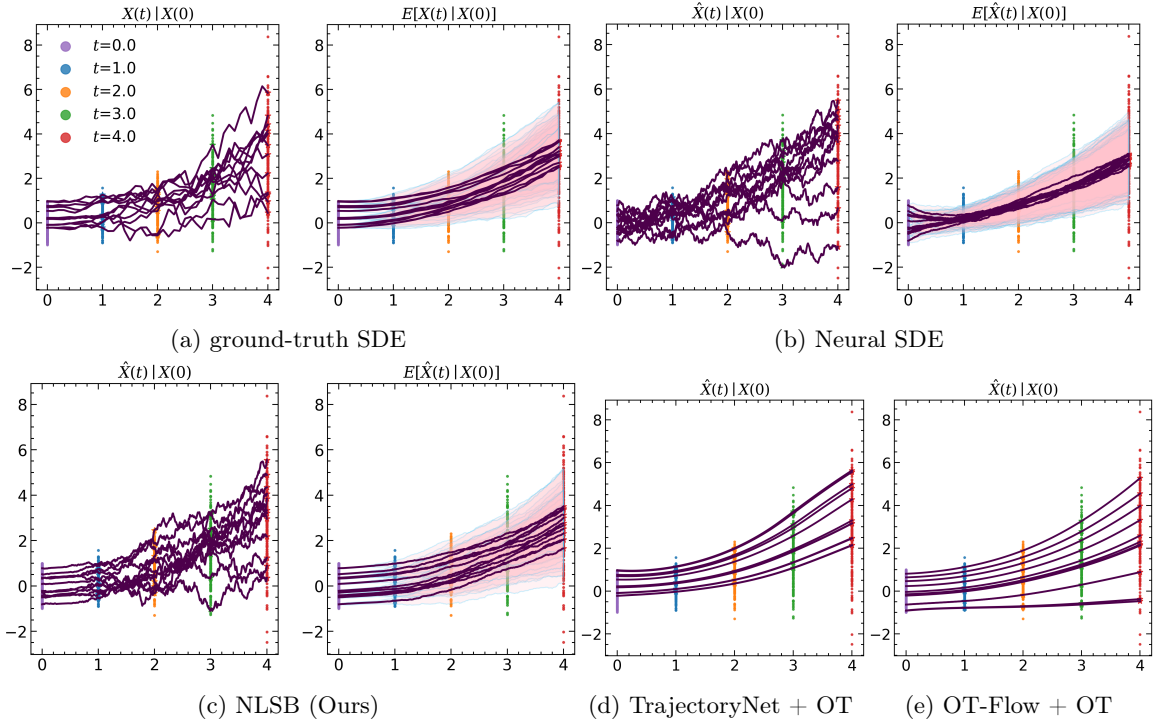


Figure 2: 1D OU process data and predictions. The five colored point clouds in the background are the ground-truth data given at each time point. The pink area and the light blue line are the one-sigma empirical confidence intervals and their boundaries for each trajectory, respectively. All trajectories were generated by all-step prediction from the initial samples at the time $t = 0$.

probability measures predicted by using the model trained on all data and trained on the data \mathcal{D}_{-t_k} , in the interval $[t_{k-1}, t_{k+1}]$. Larger CDD between them around the excluded time point t_k indicates poorer performance in interpolating sample trajectories. For the calculations of MDD and CDD, we used not only EMD-L2 but also EMD-L1 to more accurately measure the distance between distributions with a wide base. When evaluating the SDE-based methods, we calculated the mean and standard deviation of 100 MDD scores.

Results

Table 2 shows that the SDE-based methods can predict population-level dynamics with a comparable or better performance against all existing ODE-based methods, even for high-dimensional real data. In particular, the SDE-based methods significantly outperform the ODE-based ones in predicting the transitions where the samples from t_1 to t_2 and from t_3 to t_4 are highly diffuse, indicating that the explicit modeling of diffusion is effective. (see Figure 5 in Appendix E). Overall, the standard deviation of the MDD values is smaller for NLSB than for neural SDE, demonstrating less variation in the approximation accuracy of the marginal distribution. Table 3 shows that NLSB generates robust trajectories with and without data at the intermediate time point than neural SDE. This result suggests that the LSB-based regularization helps interpolate trajectories. See the Appendix E for a visualization of trajectories with uncertainty.

Table 2: Evaluation results for population-level dynamics at time of observation for scRNA-seq data. The MDD value at t_k is computed between the ground-truth and the samples predicted from the previous ground-truth samples at t_{k-1} for each $k = 1, 2, 3$ and 4.

MDD (EMD-L2) ↓	t_1	t_2	t_3	t_4
Neural SDE	0.62 ± 0.018	0.78 ± 0.024	0.77 ± 0.017	0.75 ± 0.016
NLSB (Ours)	0.64 ± 0.017	0.77 ± 0.019	0.77 ± 0.013	0.76 ± 0.012
OT-Flow	0.74	0.96	0.93	0.95
OT-Flow + OT	0.75	0.93	0.93	0.88
TrajectoryNet	0.64	0.87	0.78	0.89
TrajectoryNet + OT	0.66	0.87	0.78	0.97

MDD (EMD-L1) ↓	t_1	t_2	t_3	t_4
Neural SDE	1.11 ± 0.030	1.40 ± 0.046	1.38 ± 0.030	1.34 ± 0.025
NLSB (Ours)	1.15 ± 0.028	1.40 ± 0.035	1.38 ± 0.023	1.36 ± 0.019
OT-Flow	1.31	1.73	1.68	1.69
OT-Flow + OT	1.33	1.65	1.69	1.56
TrajectoryNet	1.15	1.60	1.42	1.58
TrajectoryNet + OT	1.20	1.60	1.41	1.72

Table 3: Mean value of CDD evaluated at 7 equally spaced time points within time period $[t_{k-1}, t_{k+1}]$ around excluded time point t_k for each $k = 1, 2$ and 3. The CDD value at the time $t \in [t_{k-1}, t_{k+1}]$ was computed between the two groups of predicted samples generated from the previous samples at t_{k-1} using the model trained on all data and the data \mathcal{D}_{-t_k} .

Mean CDD (EMD-L2 EMD-L1) ↓	$[t_0, t_2]$	$[t_1, t_3]$	$[t_2, t_4]$
Neural SDE	1.30 2.47	0.79 1.40	0.82 1.47
NLSB (Ours)	0.72 1.30	0.66 1.18	0.70 1.26

6 Conclusion

We demonstrated that NLSB can estimate the population-level dynamics with the same or better performance than existing methods and that the prior knowledge introduced by the Lagrangian is effective in estimating more accurate trajectories of individual samples in the populations. Future work includes developing methods that can handle reaction phenomena with advection and diffusion phenomena.

Acknowledgments

We thank the lab members for their discussions and inspiration for our research.

References

- [1] Jean-David Benamou and Yann Brenier. A computational fluid mechanics solution to the monge-kantorovich mass transfer problem. *Numerische Mathematik*, 84(3):375–393, 2000.
- [2] Charlotte Bunne, Laetitia Meng-Papaxanthos, Andreas Krause, and Marco Cuturi. Jkonet: Proximal optimal transport modeling of population dynamics. *arXiv preprint arXiv:2106.06345*, 2021.
- [3] Kenneth Caluya and Abhishek Halder. Wasserstein proximal algorithms for the schrödinger bridge problem: Density control with nonlinear drift. *IEEE Transactions on Automatic Control*, 2021.
- [4] Ricky TQ Chen, Yulia Rubanova, Jesse Bettencourt, and David K Duvenaud. Neural ordinary differential equations. *Advances in neural information processing systems*, 31, 2018.
- [5] Paolo Dai Pra. A stochastic control approach to reciprocal diffusion processes. *Applied mathematics and Optimization*, 23(1):313–329, 1991.
- [6] Lawrence C Evans. An introduction to mathematical optimal control theory version 0.2. *Lecture notes available at <http://math.berkeley.edu/~evans/control.course.pdf>*, 1983.
- [7] Chris Finlay, Jörn-Henrik Jacobsen, Levon Nurbekyan, and Adam Oberman. How to train your neural ode: the world of jacobian and kinetic regularization. In *International conference on machine learning*, pages 3154–3164. PMLR, 2020.
- [8] Mike Fisher, Jorge Nocedal, Yannick Trémolet, and Stephen J Wright. Data assimilation in weather forecasting: a case study in pde-constrained optimization. *Optimization and Engineering*, 10(3):409–426, 2009.
- [9] Will Grathwohl, Ricky TQ Chen, Jesse Bettencourt, Ilya Sutskever, and David Duvenaud. Ffjord: Free-form continuous dynamics for scalable reversible generative models. In *International Conference on Learning Representations*, 2018.
- [10] Tatsunori Hashimoto, David Gifford, and Tommi Jaakkola. Learning population-level diffusions with generative rnns. In *International Conference on Machine Learning*, pages 2417–2426. PMLR, 2016.
- [11] Desmond J Higham. An algorithmic introduction to numerical simulation of stochastic differential equations. *SIAM review*, 43(3):525–546, 2001.
- [12] Benton Jamison. The markov processes of schrödinger. *Zeitschrift für Wahrscheinlichkeitstheorie und Verwandte Gebiete*, 32(4):323–331, 1975.
- [13] Patrick Kidger, James Foster, Xuechen Li, and Terry J Lyons. Neural sdes as infinite-dimensional gans. In *International Conference on Machine Learning*, pages 5453–5463. PMLR, 2021.
- [14] AN Kolomgorov, IG Petrovskii, and NS Piskunov. Study of a diffusion equation that is related to the growth of a quality of matter, and its application to a biological problem, byul. *Mosk. Gos. Univ. Ser. A Mat. Mekh*, 1(1):26, 1937.
- [15] Xuechen Li, Ting-Kam Leonard Wong, Ricky TQ Chen, and David Duvenaud. Scalable gradients for stochastic differential equations. In *International Conference on Artificial Intelligence and Statistics*, pages 3870–3882. PMLR, 2020.

- [16] Kenneth G Manton, XiLiang Gu, and Gene R Lowrimore. Cohort changes in active life expectancy in the us elderly population: Experience from the 1982–2004 national long-term care survey. *The Journals of Gerontology Series B: Psychological Sciences and Social Sciences*, 63(5): S269–S281, 2008.
- [17] Toshio Mikami. Variational processes from the weak forward equation. *Communications in mathematical physics*, 135(1):19–40, 1990.
- [18] Kevin R Moon, David van Dijk, Zheng Wang, Scott Gigante, Daniel B Burkhardt, William S Chen, Kristina Yim, Antonia van den Elzen, Matthew J Hirn, Ronald R Coifman, et al. Visualizing structure and transitions in high-dimensional biological data. *Nature biotechnology*, 37(12):1482–1492, 2019.
- [19] Derek Onken, S Wu Fung, Xingjian Li, and Lars Ruthotto. Ot-flow: Fast and accurate continuous normalizing flows via optimal transport. In *Proceedings of the AAAI Conference on Artificial Intelligence*, volume 35, 2021.
- [20] Michele Pavon and Anton Wakolbinger. On free energy, stochastic control, and schrödinger processes. In *Modeling, Estimation and Control of Systems with Uncertainty*, pages 334–348. Springer, 1991.
- [21] Geoffrey Schiebinger, Jian Shu, Marcin Tabaka, Brian Cleary, Vidya Subramanian, Aryeh Solomon, Joshua Gould, Siyan Liu, Stacie Lin, Peter Berube, et al. Optimal-transport analysis of single-cell gene expression identifies developmental trajectories in reprogramming. *Cell*, 176(4):928–943, 2019.
- [22] Yang Song, Jascha Sohl-Dickstein, Diederik P Kingma, Abhishek Kumar, Stefano Ermon, and Ben Poole. Score-based generative modeling through stochastic differential equations. In *International Conference on Learning Representations*, 2020.
- [23] Alexander Tong, Jessie Huang, Guy Wolf, David Van Dijk, and Smita Krishnaswamy. Trajectory-rinet: A dynamic optimal transport network for modeling cellular dynamics. In *International Conference on Machine Learning*, pages 9526–9536. PMLR, 2020.
- [24] Belinda Tzen and Maxim Raginsky. Neural stochastic differential equations: Deep latent gaussian models in the diffusion limit. *arXiv preprint arXiv:1905.09883*, 2019.
- [25] Belinda Tzen and Maxim Raginsky. Theoretical guarantees for sampling and inference in generative models with latent diffusions. In *Conference on Learning Theory*, pages 3084–3114. PMLR, 2019.
- [26] Karren D Yang and Caroline Uhler. Scalable unbalanced optimal transport using generative adversarial networks. In *International Conference on Learning Representations*, 2018.
- [27] Liu Yang and George Em Karniadakis. Potential flow generator with l_2 optimal transport regularity for generative models. *IEEE Transactions on Neural Networks and Learning Systems*, 2020.

A Derivation of Neural Lagrangian Schrödinger bridge

We consider the time-evolving density p_t governed by the Fokker-Planck equation over the bounded domain $D \subset \mathbb{R}^d$. The domain D satisfies the no-flux condition:

$$\mathbf{f}_t \cdot \mathbf{n} = 0 \quad \text{on} \quad \partial D \times [t_0, t_1], \quad (11)$$

where \mathbf{n} is the unit outward normal vector to the boundary of D . We will solve the SOT problem as shown in Eq., (4) by reformulating it as a saddle point problem for $(p_t, \mathbf{m}_t) := (p_t, p_t \mathbf{f}_t)$. Let us define the Lagrangian \mathcal{L} with the time-space-dependent Lagrange multiplier $\Phi(\mathbf{x}, t)$.

$$\begin{aligned} \mathcal{L}(\Phi, p, \mathbf{m}) &:= \int_{t_0}^{t_1} \int_D L\left(t, \mathbf{x}, \frac{\mathbf{m}_t}{p_t}\right) p_t(\mathbf{x}) + \Phi(\mathbf{x}, t) \left(\partial_t p_t + \operatorname{div}(\mathbf{m}_t) - \sum_{i,j}^d \frac{\partial^2}{\partial x_i \partial x_j} [D_{i,j}(\mathbf{x}, t) p_t(\mathbf{x})] \right) d\mathbf{x} dt, \\ &= \int_t \int_D L\left(t, \mathbf{x}, \frac{\mathbf{m}_t}{p_t}\right) p_t + \int_t \int_D \left(\partial_t \Phi(\mathbf{x}, t) + \frac{1}{2} \sum_{i,j}^d D_{i,j} [\nabla_{\mathbf{x}}^2 \Phi(\mathbf{x}, t)]_{i,j} \right) p_t + \mathbf{m}_t(\mathbf{x}) \cdot \nabla_{\mathbf{x}} \Phi(\mathbf{x}, t) \\ &\quad - \int_D \Phi(\mathbf{x}, t_1) p(\mathbf{x}, t_1) + \int_D \Phi(\mathbf{x}, t_0) p(\mathbf{x}, t_0). \end{aligned}$$

We can rewrite the SOT problem as:

$$\inf_{p, \mathbf{m}} \sup_{\Phi} \mathcal{L}(p, \mathbf{m}, \Phi). \quad (12)$$

The saddle point $(p^*, \mathbf{m}^*, \Phi^*)$ of the problem in Eq., (12) satisfies the following condition:

$$\begin{aligned} \partial_{\Phi} \mathcal{L}|_{(p^*, \mathbf{m}^*, \Phi^*)} = 0 &\Leftrightarrow \begin{cases} \partial_t p_t^* + \operatorname{div}(\mathbf{m}_t^*) - \sum_{i,j}^d \frac{\partial^2}{\partial x_i \partial x_j} [D_{i,j}(\mathbf{x}, t) p_t^*] = 0 \\ p^*(\cdot, t_0) = \mu_0, \quad p^*(\cdot, t_1) = \mu_1 \end{cases}, \\ \partial_p \mathcal{L}|_{(p^*, \mathbf{m}^*, \Phi^*)} = 0 &\Leftrightarrow \begin{cases} \partial_t \Phi^* + \frac{1}{2} \sum_{i,j}^d D_{i,j}(\mathbf{x}, t) [\nabla_{\mathbf{x}}^2 \Phi(\mathbf{x}, t)]_{i,j} - h(\mathbf{x}, t) = 0 \\ h(\mathbf{x}, t) = L\left(t, \mathbf{x}, \frac{\mathbf{m}^*}{p^*}\right) - \nabla_{\mathbf{u}} L(t, \mathbf{x}, \mathbf{u})|_{\mathbf{u}=\frac{\mathbf{m}^*}{p^*}}^{\top} \left(\frac{\mathbf{m}^*}{p^*}\right) \end{cases}, \\ \partial_{\mathbf{m}} \mathcal{L}|_{(p^*, \mathbf{m}^*, \Phi^*)} = 0 &\Leftrightarrow \nabla_{\mathbf{u}} L(t, \mathbf{x}, \mathbf{u})|_{\mathbf{u}=\frac{\mathbf{m}^*}{p^*}} = -\nabla_{\mathbf{x}} \Phi^*. \end{aligned}$$

Therefore, the optimal drift function is given by $\mathbf{f}^* = \frac{\mathbf{m}^*}{p^*} = [\nabla_{\mathbf{u}} L]^{-1}(-\nabla_{\mathbf{x}} \Phi)$ and the potential function Φ is the solution of the HJB equation:

$$\partial_t \Phi(\mathbf{x}, t) + \frac{1}{2} \sum_{i,j}^d D_{i,j}(\mathbf{x}, t) [\nabla_{\mathbf{x}}^2 \Phi(\mathbf{x}, t)]_{i,j} - L(t, \mathbf{x}, \mathbf{f}^*) + \nabla_{\mathbf{u}} L(t, \mathbf{x}, \mathbf{u})|_{\mathbf{u}=\mathbf{f}^*}^{\top} \mathbf{f}^*(\mathbf{x}, t) = 0$$

B Model architecture

The model structure of the potential function proposed in OT-Flow [19] is shown below.

$$\begin{aligned} \Phi(\mathbf{s}) &= \mathbf{w}^{\top} N(\mathbf{s}; \{\mathbf{K}_i, \mathbf{b}_i\}_{0 \leq i \leq M}) + \frac{1}{2} \mathbf{s}^{\top} (\mathbf{A}^{\top} \mathbf{A}) \mathbf{s} + \mathbf{b}^{\top} \mathbf{s} + c, \\ N(\mathbf{s}; \{\mathbf{K}_i, \mathbf{b}_i\}_{0 \leq i \leq M}) &= \mathbf{u}_M, \\ \mathbf{u}_i &= \mathbf{u}_{i-1} + h\sigma(\mathbf{K}_i \mathbf{u}_{i-1} + \mathbf{b}_i) \quad (1 \leq i \leq M), \quad \mathbf{u}_0 = \sigma(\mathbf{K}_0 \mathbf{s} + \mathbf{b}_0), \end{aligned}$$

where $\mathbf{s} = (\mathbf{x}, t)$ is input vector, $\mathbf{w}, \{\mathbf{K}_i, \mathbf{b}_i\}_{0 \leq i \leq M}$, $\mathbf{A}, \mathbf{b}, c$ are learnable parameters, h is fixed step size, and the activation function is defined as $\sigma(\mathbf{x}) = \log(\exp(\mathbf{x}) + \exp(-\mathbf{x}))$.

The gradient of the potential is described as follows:

$$\begin{aligned}\nabla_{\mathbf{s}} \Phi(\mathbf{s}) &= \nabla_{\mathbf{s}} N(\mathbf{s}; \{\mathbf{K}_i, \mathbf{b}_i\}_{0 \leq i \leq M}) \mathbf{w} + (\mathbf{A}^\top \mathbf{A}) \mathbf{s} + \mathbf{b}, \\ \nabla_{\mathbf{s}} N(\mathbf{s}; \{\mathbf{K}_i, \mathbf{b}_i\}_{0 \leq i \leq M}) &= \mathbf{K}_0^\top \text{diag}(\sigma'(\mathbf{K}_0 \mathbf{s} + \mathbf{b}_0)) \mathbf{z}_1, \\ \mathbf{z}_i &= \mathbf{z}_{i+1} + h \mathbf{K}_i^\top \text{diag}(\sigma'(\mathbf{K}_i \mathbf{u}_{i-1} + \mathbf{b}_i)) \mathbf{z}_{i+1} \quad (1 \leq i \leq M), \quad \mathbf{z}_{M+1} = \mathbf{1}.\end{aligned}$$

We can write σ' down as \tanh since σ is defined as above.

Finally, the diagonal component of the potential function Hessian is shown below:

$$\begin{aligned}\nabla_{\mathbf{s}}^2 \Phi(\mathbf{s}) &= \nabla_{\mathbf{s}} (\mathbf{K}_0^\top \text{diag}(\sigma'(\mathbf{K}_0 \mathbf{s} + \mathbf{b}_0)) \mathbf{z}_1) + h \sum_{i=1}^M (\nabla_{\mathbf{s}} \mathbf{u}_{i-1}^\top \nabla_{\mathbf{s}} (\mathbf{K}_i^\top \text{diag}(\sigma'(\mathbf{K}_i \mathbf{u}_{i-1} + \mathbf{b}_i)) \mathbf{z}_{i+1}) \nabla_{\mathbf{s}} \mathbf{u}_{i-1}^\top) \\ &= \mathbf{K}_0^\top \text{diag}(\sigma''(\mathbf{K}_0 \mathbf{s} + \mathbf{b}_0) \odot \mathbf{z}_1) \mathbf{K}_0 + \nabla_{\mathbf{s}} \mathbf{u}_{i-1}^\top \mathbf{K}_i^\top \text{diag}(\sigma''(\mathbf{K}_i \mathbf{u}_{i-1} + \mathbf{b}_i) \odot \mathbf{z}_{i+1}) \mathbf{K}_i \nabla_{\mathbf{s}} \mathbf{u}_{i-1}^\top, \\ [\nabla_{\mathbf{s}}^2 \Phi(\mathbf{s})]_{i,i} &= [(\sigma''(\mathbf{K}_0 \mathbf{s} + \mathbf{b}_0) \odot \mathbf{z}_1)^\top (\mathbf{K}_0 \odot \mathbf{K}_0)]_i \\ &\quad + h \sum_{i=1}^M [(\sigma''(\mathbf{K}_i \mathbf{u}_{i-1} + \mathbf{b}_i) \odot \mathbf{z}_{i+1})^\top (\mathbf{K}_i \nabla_{\mathbf{s}} \mathbf{u}_{i-1}^\top \odot \mathbf{K}_i \nabla_{\mathbf{s}} \mathbf{u}_{i-1}^\top)]_i,\end{aligned}$$

where \odot is element-wise product, $\nabla_{\mathbf{s}} \mathbf{u}_i$ can be obtained using the following update equation:

$$\nabla_{\mathbf{s}} \mathbf{u}_i^\top \leftarrow \nabla_{\mathbf{s}} \mathbf{u}_{i-1}^\top + \text{diag}(h \sigma'(\mathbf{K}_i \mathbf{u}_{i-1} + \mathbf{b}_i)) \mathbf{K}_i \nabla_{\mathbf{s}} \mathbf{u}_{i-1}^\top.$$

C Schrödinger bridge and Stochastic optimal control

We briefly provide a connection between SB problem and SOC problem.

Definition 2 (SB problem; [12]). Let $\Omega = C([0, T], \mathbb{R}^d)$ be the space of \mathbb{R}^d -valued continuous functions on time interval $[0, T]$. Denote $\mathcal{P}(\Omega)$ as the probability measures space on the path space Ω . SB problem is defined as follows:

$$\min_{\mathbb{Q} \in \mathcal{P}(\Omega)} D_{\text{KL}}(\mathbb{Q} \parallel \mathbb{P}), \quad \text{subject to } \mathbb{Q}_0 \sim \mu_0, \mathbb{Q}_T \sim \mu_T, \quad (13)$$

where $\mu, \nu \in \mathcal{P}(\mathbb{R}^d)$ and the relative entropy $D_{\text{KL}} = \int \log \left(\frac{d\mathbb{Q}}{d\mathbb{P}} \right) d\mathbb{Q}$ if $\mathbb{Q} \ll \mathbb{P}$, and $D_{\text{KL}} = \infty$ otherwise.

Caluya and Halder [3] showed SB optimality under the reference path measure \mathbb{P} of the following SDE:

$$d\mathbf{X}_t = \mathbf{f}(\mathbf{X}_t, t)dt + g(t)d\mathbf{W}_t, \quad (14)$$

where $\mathbf{f} : \mathbb{R}^d \times [0, T] \mapsto \mathbb{R}^d$ is the drift function, $g : [0, T] \mapsto \mathbb{R}$ is the diffusion function, and \mathbf{W}_t is standard Wiener process.

Theorem 3. Let $\Psi(\mathbf{x}, t)$ and $\hat{\Psi}(\mathbf{x}, t)$ be the solutions to the following PDEs:

$$\begin{cases} \frac{\partial \Psi}{\partial t} = -\nabla_{\mathbf{x}} \Psi^\top \mathbf{f} - \frac{1}{2} \text{Tr} \left(g^2 \nabla_{\mathbf{x}}^2 \Psi \right) \\ \frac{\partial \hat{\Psi}}{\partial t} = -\nabla_{\mathbf{x}} \cdot (\hat{\Psi} \mathbf{f}) + \frac{1}{2} \text{Tr} \left(g^2 \nabla_{\mathbf{x}}^2 \hat{\Psi} \right) \end{cases} \quad \text{s.t. } \Psi(0, \cdot) \hat{\Psi}(0, \cdot) = p_0, \Psi(T, \cdot) \hat{\Psi}(T, \cdot) = p_T, \quad (15)$$

where p_0 and p_T are the probability density of μ_0 and μ_T , respectively. Then, the solution to the SB problem (13) where \mathbb{P} is the path measure of the SDE (14) can be described by the following forward or backward SDE:

$$\begin{aligned} d\mathbf{X}_t &= \left[\mathbf{f} + g^2 \nabla_{\mathbf{x}} \log \Psi(\mathbf{X}_t, t) \right] dt + g d\mathbf{W}_t, & \mathbf{X}_0 &\sim \mu_0, \\ d\mathbf{X}_t &= \left[\mathbf{f} - g^2 \nabla_{\mathbf{x}} \log \hat{\Psi}(\mathbf{X}_t, t) \right] dt + g d\mathbf{W}_t, & \mathbf{X}_T &\sim \mu_T. \end{aligned} \quad (16)$$

Caluya and Halder [3] also showed the solution of SB problem (16) characterize the solution of the following optimization problem considered in [20, 5].

Theorem 4. *We consider the following optimization problem.*

$$\min_{\mathbf{u}} \mathbb{E} \left[\int_0^T \frac{1}{2} \|\mathbf{u}(\mathbf{X}_t, t)\|^2 dt \right] \quad (17)$$

$$s.t. \quad \begin{cases} d\mathbf{X}_t = [\mathbf{f}(\mathbf{X}_t, t) + g(t)\mathbf{u}(\mathbf{X}_t, t)] dt + \sqrt{2\epsilon}g(t)d\mathbf{W}_t \\ \mathbf{X}_0 \sim \mu_0, \quad \mathbf{X}_T \sim \mu_T, \end{cases} \quad (18)$$

where g is uniformly lower-bounded and \mathbf{f} satisfies Lipschitz conditions with at most linear growth in \mathbf{x} . The minimizer of the problem (17) is obtained by $\mathbf{u}^* = 2\epsilon g \nabla_{\mathbf{x}} \log \Psi$ where Ψ satisfies the SB optimality (15).

The problem (17) is the SOC problem with the additional terminal constraint. Theorem 4 shows the problem (17) can be regarded as another formulation of the SB problem (13).

D Experimental details

D.1 Training configuration for experiments on synthetic data

Common settings

We generated 2048 samples and 512 samples for each time point as training and validation data, respectively. We trained all models with a batch size of 512 for each time point and used the early stopping method, which monitors the EMD-L2 value on validation data. We used Adam optimizer to optimize all learnable parameters with a learning rate of 0.001 and the decay rate of $\beta_1 = 0.9$, $\beta_2 = 0.999$.

Settings for NLSB and neural SDE

For the potential model Φ_θ , we set the number of ResNet layers $M = 2$, the step size $h = 1.0$, the rank of matrix $\text{rank}(\mathbf{A}) = 10$, and the hidden dimension $m = 2$. We used a two-layer FCNN of a hidden dimension 16 for the diffusion function. The activations functions are LipSwish. We trained the neural SDE in the framework of the torchsde library³ and used the Euler-Maruyama method with the constant step size of 0.01 as an SDE solver. Backpropagation was performed without using the adjoint method. We set the weight coefficients for NLSB in Eq. 4.1 to $\lambda_e(t_0, t_1) = 0.32$, $\lambda_h(t_0, t_1) = 0.16$, $\lambda_e(t_1, t_2) = 0.006$, $\lambda_h(t_1, t_2) = 0.007$, $\lambda_e(t_2, t_3) = 0.001$, $\lambda_h(t_2, t_3) = 0.001$, $\lambda_e(t_3, t_4) = 0.0001$, $\lambda_h(t_3, t_4) = 0.0001$.

³<https://github.com/google-research/torchsde>

Settings for TrajectoryNet

We used three concatsquash layers of a hidden dimension 16 with hyperbolic tangent activations to model the velocity function \mathbf{v} . A concatsquash layer cs is defined in the released code of FFJORD [9] as:

$$\text{cs}(\mathbf{x}, t) = (\mathbf{W}_x \mathbf{x} + \mathbf{b}_x) \sigma(\mathbf{W}_t t + \mathbf{b}_t) + (\mathbf{W}_b t + \mathbf{b}_b), \quad (19)$$

where σ is the sigmoid function, and \mathbf{W}_x , \mathbf{W}_t , \mathbf{W}_b , \mathbf{b}_x , \mathbf{b}_t , \mathbf{b}_b are all learnable parameters. We trained the model with torchdiffeq library⁴ and used the dopri5 solver with both absolute and relative tolerances set to 10^{-5} . In the training for TrajectoryNet with OT-based regularization, we set the weight coefficients to $\tilde{\lambda}_e(t_0, t_1) = \tilde{\lambda}_e(t_1, t_2) = 0.35$, $\tilde{\lambda}_e(t_2, t_3) = \tilde{\lambda}_e(t_3, t_4) = 0.002$.

Settings for OT-Flow

We used the same potential model Φ in NLSB and neural SDE with the same hyperparameters. We trained the model with torchdiffeq library. We used the Euler method as the ODE solver with a constant step size of 0.01 and both absolute and relative tolerances set to 10^{-5} . In the training for OT-Flow with OT-based regularization, we set the weight coefficients to $\tilde{\lambda}_e(t_0, t_1) = \tilde{\lambda}_e(t_1, t_2) = 0.1$, $\tilde{\lambda}_h(t_0, t_1) = \tilde{\lambda}_h(t_1, t_2) = 0.01$, $\tilde{\lambda}_e(t_2, t_3) = \tilde{\lambda}_e(t_3, t_4) = 0.001$, $\tilde{\lambda}_h(t_2, t_3) = \tilde{\lambda}_h(t_3, t_4) = 0.001$.

D.2 Training configuration for experiments on scRNA-seq data

Common settings

We used Adam optimizer for training all methods with learning rate 0.001 and the decay rate $\beta_1 = 0.9$, $\beta_2 = 0.999$. We trained all models with a batch size of 1000 for each time point and used the early stopping method, which monitors the EMD-L2 value on the validation data.

Settings for NLSB and neural SDE

In the NLSB and neural SDE training, all settings for the potential model and the SDE solver are the same as in Appendix D.1. We set the noise type to diagonal and the weight coefficients for NLSB to $\lambda_e(t_0, t_1) = \lambda_e(t_1, t_2) = 0.01$, $\lambda_h(t_0, t_1) = \lambda_h(t_1, t_2) = 0.01$, $\lambda_e(t_2, t_3) = \lambda_e(t_3, t_4) = 0.01$, $\lambda_h(t_2, t_3) = \lambda_h(t_3, t_4) = 0.001$.

Settings for TrajectoryNet

We used the velocity model with 64 hidden dimensions. Other settings for the velocity model and all settings for the ODE solver are the same as those shown in Appendix D.1. We set the OT-based regularization coefficients to $\tilde{\lambda}_e(t_0, t_1) = \tilde{\lambda}_e(t_1, t_2) = 0.01$, $\tilde{\lambda}_e(t_2, t_3) = \tilde{\lambda}_e(t_3, t_4) = 0.1$.

Settings for OT-Flow

All settings for the potential model and the solver are the same as in Appendix D.1. We set the OT-based regularization coefficients to $\tilde{\lambda}_e(t_0, t_1) = \tilde{\lambda}_e(t_1, t_2) = 0.01$, $\tilde{\lambda}_h(t_0, t_1) = \tilde{\lambda}_h(t_1, t_2) = 0.01$, $\tilde{\lambda}_e(t_2, t_3) = \tilde{\lambda}_e(t_3, t_4) = 0.001$, $\tilde{\lambda}_h(t_2, t_3) = \tilde{\lambda}_h(t_3, t_4) = 0.01$.

⁴<https://github.com/rtqichen/torchdiffeq>

E Additional experimental results

The time evolution of the distribution for a single sample is visualized as a heat map in Figure 3. The trajectories are visualized in Figure 4 and the sample population in Figure 5. All figures are visualizations in the space of the first and second principal components. The x-axis represents the first principal component and the y-axis the second principal component.

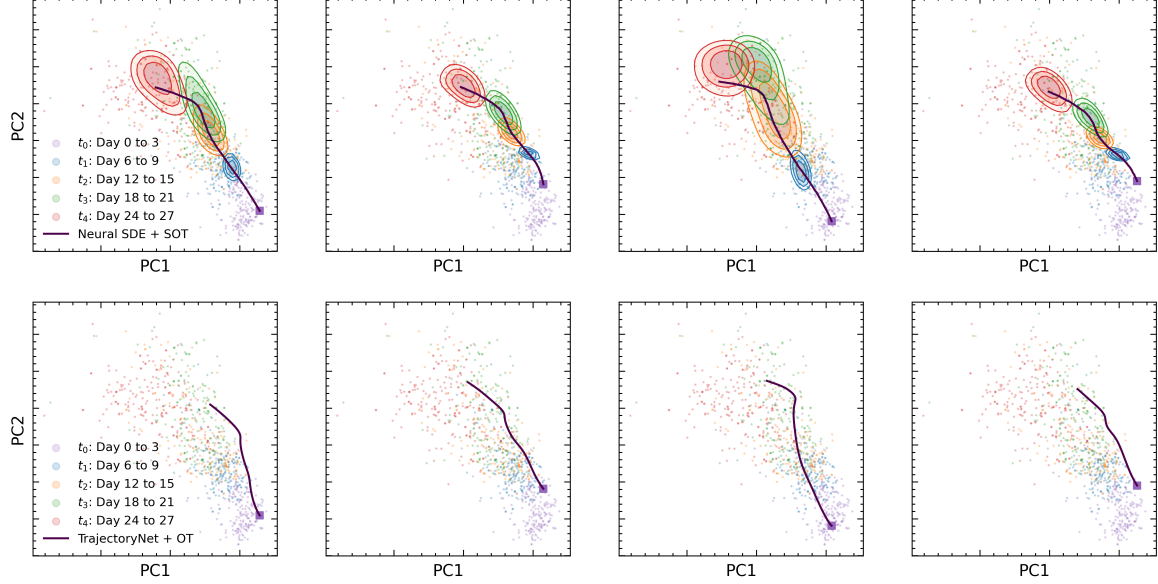


Figure 3: Visualization of the time evolution for a single sample on scRNA-seq data. The upper and lower images are predictions from the same initial sample at t_0 , with the upper row predicted by NLSB and the lower row predicted by TrajectoryNet + OT. The color gradients depict the magnitude of the probability density. The probability density function is estimated by kernel density estimation using Gaussian kernels.

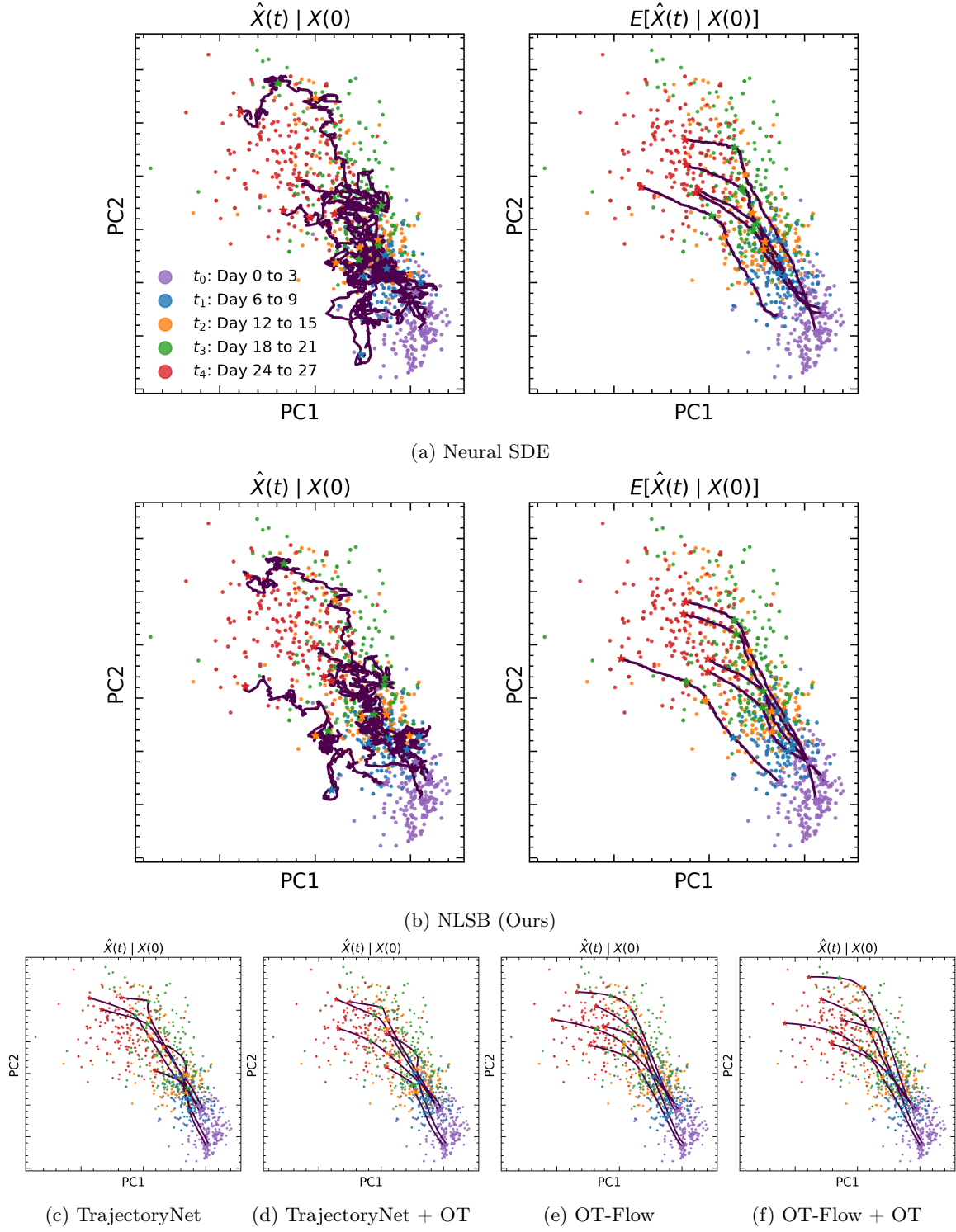


Figure 4: scRNA-seq data and predictions. The x- and y-axes denote the first and second principal components, respectively. The five colored point clouds in the background are the ground-truth data given at each time point. All five trajectories are generated by all-step prediction from the initial samples at t_0 .

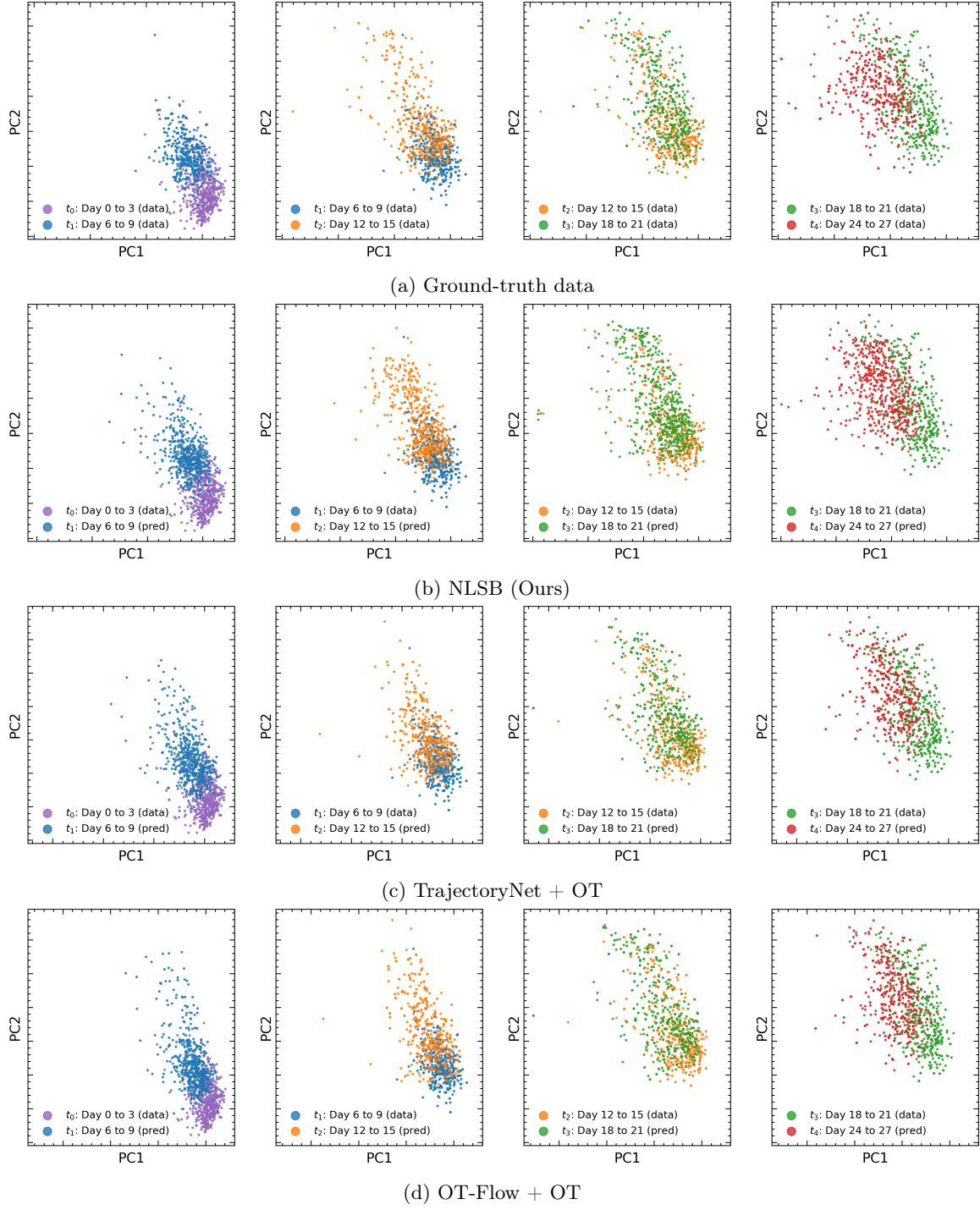


Figure 5: Visualization of the ground-truth data and one-step ahead sample prediction on scRNA-seq data.